

Solving the Gross-Pitaevskii Equation with Quantic Tensor Trains: Ground States and Nonlinear Dynamics

Qian-Can Chen¹, I-Kang Liu², Jheng-Wei Li³, and Chia-Min Chung^{1,4,5,6*},

¹ Department of Electrophysics, National Yang Ming Chiao Tung University, Hsinchu 300, Taiwan

² School of Mathematics, Statistics and Physics, Newcastle University, Newcastle upon Tyne, NE1 7RU, United Kingdom

³ Université Grenoble Alpes, CEA, Grenoble INP, IRIG, Pheliqs, F-38000 Grenoble, France

⁴ Physics Division, National Center for Theoretical Sciences, Taipei 10617, Taiwan

⁵ Department of Physics, National Sun Yat-sen University, Kaohsiung 80424, Taiwan

⁶ Center for Theoretical and Computational Physics, National Yang Ming Chiao Tung University, Hsinchu 300093, Taiwan

* chiaminchung@gmail.com

Abstract

We develop a tensor network framework based on the quantic tensor train (QTT) format to efficiently solve the Gross-Pitaevskii equation (GPE), which governs Bose-Einstein condensates under mean-field theory. For sufficiently regular functions, the QTT approach enables exponentially fine grids with computational cost that grows only linearly. By adapting the time-dependent variational principle (TDVP) and gradient descent methods, we accurately handle the GPE's nonlinearities within the QTT structure. Our approach enables high-resolution simulations with drastically reduced computational cost on highly refined grids. We benchmark the ground states and dynamics of BECs, including vortex lattice formation and breathing modes, demonstrating superior performance over regular-grid-based methods and stable long-time evolution due to saturating bond dimensions. This establishes QTT as a powerful tool for nonlinear quantum simulations.

Copyright attribution to authors.

This work is a submission to SciPost Physics.

License information to appear upon publication.

Publication information to appear upon publication.

Received Date

Accepted Date

Published Date

Contents

1	Introduction	2
2	Gross-Pitaevskii equation	4
3	Methods	5
3.1	Imaginary-time evolution: TDVP	5
3.2	Variational method: gradient descent	6
4	Benchmark	7
4.1	Two-dimensional BEC in a harmonic potential	7

4.2 Rotating BEC	9
4.3 Dynamics	12
5 Conclusion and Discussion	12
A Normalization	14
B Review of Quantic Tensor Train	14
C Exact QTT representations	16
D Convergence behavior	18
D.1 BEC in a harmonic trap	18
D.2 Vortex systems	19
D.3 Effect of meshgrid resolution	20
References	21

1 Introduction

Efficient numerical representations of high-dimensional data are essential in both quantum many-body physics and applied mathematics [1, 2]. Tensor network methods provide a systematic approach to compressing such data while preserving essential correlations. Matrix product states (MPS), in particular, have been widely used to approximate low-entanglement quantum states, enabling accurate simulations of low-dimensional quantum systems [3, 4]. In applied mathematics, an analogous approach is the tensor train (TT) decomposition, which shares the same mathematical structure as MPS and is widely used for efficiently representing high-dimensional data [5–7].

A key extension of tensor train decomposition is the quantic tensor train (QTT), a quantum-inspired numerical method that efficiently discretizes continuous functions on an exponential grid. A QTT maps high-dimensional tensors into a logarithmic-size tensor train, which significantly reduces storage requirements and computational complexity from exponential to polynomial [8, 9]. Unlike conventional grid-based discretization techniques¹, QTT exploits a hierarchical structure similar to quantum wavefunction representations, where different "qubits" correspond to different length scales. Consequently, the tensor ranks for smooth functions are typically small. The ability to encode large-scale problems makes QTT powerful for various applications, including Fourier transforms [10, 11], quantum field theory [12–14], partial differential equations [15, 16], quantum chemistry [17], and data compression [18, 19].

Since QTT can efficiently represent continuous-space functions and operators, it is particularly useful for solving quantum systems involving single particles or systems under the mean-field approximations [20, 21]. Given that MPS and QTT essentially share the same tensor network structure but differ in their applications, numerical algorithms developed for many-body wavefunctions, such as the density matrix renormalization group (DMRG) [3, 4], can be applied naturally to QTT wavefunctions. Similarly, time evolutions of QTT wavefunctions can be effectively performed using the time-dependent variational principle (TDVP) [22, 23].

¹In our paper, the "conventional" specifically refers to the method with regular finite-difference discretization, which, at least conceptually, saves the data of all the grid points in memory.

In this work, we are particularly interested in the applications of solving the Gross-Pitaevskii equation (GPE) [24], a non-linear Schrödinger equation describing behaviors of Bose-Einstein condensates (BECs), where a large fraction of particles condense onto a single quantum state [25], under the mean-field approximation. BECs have been experimentally realised in the highly tunable ultra-cold dilute gas systems in a variety of settings with the state-of-the-art experimental technologies, e.g. [26–37]. This allows researchers to study the dynamics of macroscopic wavefunction, collective quasi-particle excitations, topological excitations, quantum turbulences, etc. [28, 38, 39], which have been successfully captured by the GPE. BEC systems are closely related superfluidity, and the emergence of quantum vortices is one of the hallmarks of that. Vortices are the angular momentum carriers in superfluid systems and can be generated by, for example, rotation [29], external stirring [32] or atom-light coupling [35]. In addition, the high tunability, precise controllability, and advanced experimental techniques make BEC systems ideal candidates for quantum simulation [39, 40] and emerging atomtronic applications [39, 41].

Typically, there are two types of problems in solving the GPE: the nonlinear eigensolutions and the time propagation of it (see Ref. [42] for a comprehensive review). A recent review for the former can be found in Ref. [43], and it is often referred to as the lowest-energy solution of a GPE [44]. A common method is known as the imaginary-time evolution/propagation (ITE) method [42, 45], evolving the wavefunction toward the lowest energy solution as the evolution of GPE in the imaginary time is sufficiently long, but it often converges slowly and needs attention for the numerical accuracy when local minimum and energy degeneracy appear. Hence, the gradient-flow [44, 46–50] and Newton [51, 52] methods have been adapted as more efficient and accurate approaches and have potential to study excited BEC states, showing fascinating physical features, such as solitonic solutions [47], engineered quantum vortices and high-orbit BEC in optical lattices [51, 53]. The spatial derivatives in the GPE can be coped with by the finite difference and pseudo-spectral methods [50, 54]. The common bases in the pseudo-spectral methods are the plane-wave and Hermite-Gaussian bases [55–57], depending on setups and system geometries. For the cases of finite difference and Fourier pseudo-spectral method, a homogeneous meshgrid is generally required, and hence one needs sufficient grid resolution to resolve the characteristic length scale to avoid numerical errors. Adaptive meshgrid method has also been implemented for a GPE-like nonlinear equation [58].

The time-evolution problem is commonly associated with the ITE method and studies on fundamental excitations of BECs [28], nonlinear dynamics, such as mode-mixings [59], superfluid turbulences and non-equilibrium dynamics [60]. A common challenge is the requirement for long-time propagation in a large grid, e.g. [58, 60–63]. The backward/forward Euler [54, 64], time-splitting [44, 58, 60, 65], Runge-Kutta and Crank-Nicolson [54, 65–68] methods have been adapted to solve the GPE.

A variety of GPE solvers exists in the literature, e.g., BEC2HPC [50], GPELab [54, 69], GPUE [70], BEC-GP-ROT-OMP [67], in addition to the works addressed previously and their associated references. However, for large-scale systems accommodating multiple vortices, accurate numerical simulations require sufficiently fine spatial discretisation, presenting significant computational challenges. Similar difficulties arise in large-scale simulations of nonlinear Schrödinger equations in cosmological [58, 71–73] and astrophysical systems [63, 74, 75], where physics at vastly different length scales are importantly related. The QTT framework effectively addresses these issues by enabling an exponential increase in discretisation points.

Due to the intrinsic nonlinearity of the GPE, standard MPS methods, such as DMRG and TDVP, cannot be applied directly without modifications. We extend existing MPS algorithms to incorporate the nonlinearities of the GPE, allowing us to efficiently compute its ground states and dynamical evolution. To find the ground states, we consider two numerical approaches: ITE [42, 45], and variational methods. We investigate the efficiency and accuracy of

the ground-state solutions of a cylindrically harmonically trapped BEC in two dimensions with and without rotation. Rotating a BEC results in the formation of quantum vortices, which organise themselves into a triangular lattice format, similar to the Abrikosov lattice in superconductors [76]. For real-time dynamics, we consider the breathing-mode excitation, a BEC width oscillation with a trapping-frequency-dependent frequency for a sufficiently large BEC [68, 77, 78], which can be generated by a sudden quench in the interaction strength. We show that the breathing-mode excitation can be accurately found in the real-time dynamics.

Our results show that QTT methods significantly speed up calculations compared to conventional methods with grid-based discretization, especially for large discretizations. We show that, between the two ground-state methods, the variational approach is more efficient than ITE. We demonstrate that, in contrast to MPS time evolution for many-body quantum states—where the bond dimension typically grows exponentially with time—the bond dimension in the QTT representation saturates at long times. This property allows for efficient and stable simulations of long time scales.

We note that similar ideas have been explored independently in Ref. [79–81], which appeared concurrently with our work.

The structure of the paper is as follows. In Sec. 2, we define the physical systems. In Sec. 3, we explain the numerical techniques used to find ground states. Benchmark results are presented in Sec. 4. Finally, we summarize our conclusions in Sec. 5. In the Supplementary Material, we review the basic concepts of QTT and explicitly show the tensors used in the Hamiltonian.

2 Gross-Pitaevskii equation

GPE is a nonlinear Schrödinger equation describing the weakly interacting BEC under mean-field approximation. In this work, we consider BEC in a rotating harmonic trap [67]. The Hamiltonian is given by

$$\hat{H} = \hat{H}^1 + \hat{H}_{\text{int}}, \quad (1)$$

$$\hat{H}^1 = -\frac{\hbar^2}{2m} \nabla^2 + \frac{1}{2} m \omega^2 r^2 - \Omega \hat{L}_z, \quad (2)$$

$$\hat{H}_{\text{int}} = g |\psi(\mathbf{r}, t)|^2, \quad (3)$$

$$\int d^3r \psi^*(\mathbf{r}) \psi(\mathbf{r}) = 1; \quad (4)$$

where \hat{H}^1 is the one-body Hamiltonian including the kinetic energy, the harmonic trapping potential $\frac{1}{2} m \omega^2 r^2$, and the rotational term $\Omega \hat{L}_z$. \hat{H}_{int} is the interaction with strength $g = 4\pi \hbar^2 a_s N / m$, where a_s is the s -wave scattering length, N is the total particle number and m is the particle mass. Throughout this work, we consider the dimensionless Hamiltonian by adopting the characteristic scales of quantum harmonic oscillator units, $\sqrt{\hbar/m\omega}$, $1/\omega$ and $\hbar\omega$ for the length, time and energy respectively (This is equivalent to set $\hbar = 1$, $m = 1$, and $\omega = 1$). The condensate wavefunction is normalized to one. (See more detail in Appendix A).

The evolution of the wavefunction is governed by the time-dependent GPE

$$i\hbar \frac{\partial \psi(\mathbf{r}, t)}{\partial t} = \hat{H} \psi(\mathbf{r}, t). \quad (5)$$

For stationary states, the wavefunction takes the form $\psi(\mathbf{r}, t) = \psi(\mathbf{r}) e^{-i\mu t/\hbar}$, where μ is the chemical potential. This yields the time-independent GPE

$$\mu \psi(\mathbf{r}) = \hat{H} \psi(\mathbf{r}). \quad (6)$$

The ground state is defined by minimizing the energy per particle,

$$E[\psi] = E^1[\psi] + E_{\text{int}}[\psi] \quad \text{with} \quad (7)$$

$$E^1[\psi] = \int d^3\mathbf{r} \psi^*(\mathbf{r}) \hat{H}^1 \psi(\mathbf{r}); \quad (8)$$

$$E_{\text{int}}[\psi] = \frac{g}{2} \int d^3\mathbf{r} |\psi(\mathbf{r})|^4. \quad (9)$$

The interaction energy is quartic in the wavefunction due to the term $|\psi(\mathbf{r})|^4$, which introduces nonlinearity. The factor $\frac{1}{2}$ in Eq. (9) avoids double counting the interactions.

3 Methods

In this section, we introduce two methods for computing the ground state of the GPE, including the ITE and a gradient descent method. For real- or imaginary-time evolution, a so-called TDVP method is a powerful method and is widely used with the MPS/QTT framework [22, 23]. GD is effective for variationally optimizing the ground state. Here, we explain the necessary modifications to both methods to handle the nonlinear interaction term in the Hamiltonian.

In all our simulations, we use periodic boundary conditions. However, due to the harmonic trapping potential, the wavefunction decays away from the center and has a tiny amplitude (in the order of 10^{-9}) at the boundary. Therefore, the boundary effect is negligible. In determining the system size, we use the Thomas-Fermi approximation (TFA) [28, 77, 82] to estimate the radius of the ground state, and choose a domain that is large enough to ensure a vanishing wavefunction amplitude at the boundary.

3.1 Imaginary-time evolution: TDVP

ITE is a common strategy for computing the ground state of the GPE [42, 45] and can be applied to the QTT wavefunction with minor modifications. Given the wavefunction (Hamiltonian) as a QTT (QTTO), the time evolution of a small time step $\delta\tau$ can be performed by using the so-called TDVP algorithm, which projects the evolution onto the tangent space of the QTT/MPS manifold, and ensures evolution remains representable as an QTT/MPS with controlled bond dimension (see Ref. [83] for an introductory lecture note.) Although the Hamiltonian in QTTO representation is typically “long-range” in the sense that it couples qubits over large distances, TDVP operates directly on the QTTO Hamiltonian, which makes it particularly well suited for QTT time evolutions. The Hamiltonian of the GPE contains the one-body term \hat{H}^1 and the interaction term \hat{H}_{int} . The interaction term $g|\psi(\mathbf{r})|^2$ depends on the wavefunction $\psi(\mathbf{r})$, and therefore needs to be updated at each step using the evolved wavefunction from the last step. The time step $\delta\tau$ is set to be $0.5\delta x^2$ to satisfy the Courant-Friedrichs-Lewy condition and ensure the stability of the convergence.

An essential step in the TDVP algorithm is to compute the effective Hamiltonian, where the required tensor contractions are shown in Fig. 1(a). The computational cost is proportional to $dD^3D_W + d^2D^2D_W^2$, where $d = 2$ is the dimension for each qubit, and D and D_W are the bond dimensions of the wavefunction and the Hamiltonian. We keep \hat{H}^1 and \hat{H}_{int} as two QTTOs and compute their effective Hamiltonians separately. For \hat{H}^1 , the bond dimension is fixed and small, and the corresponding computational cost is relatively low. However, the QTTO for the interaction has a bond dimension D^2 for an exact calculation, where D is the bond dimension of the wavefunction. Since D controls the accuracy of the wavefunction and can be large in a challenging system, we need to compress $\psi^2(\mathbf{r})$ from a bond dimension D^2 to a smaller bond

dimension χ to achieve efficient computations (see Fig. 1(b)). The computational cost then depends on the efficiency of this compression. In this work, we perform the compression using the variational method by maximizing the overlap $\langle \psi^2 | \psi_\chi^2 \rangle$ [2], where $\psi_\chi^2(\mathbf{r})$ is the compressed $\psi^2(\mathbf{r})$ with the bond dimension χ . In practice, $\psi^2(\mathbf{r})$ typically has a structure similar to that of $\psi(\mathbf{r})$, and therefore χ is typically on the same order as D . This yields an overall computational complexity of roughly $O(D^4)$.

3.2 Variational method: gradient descent

Another powerful approach to the ground state is to use the variational method to minimize the energy $E[\psi]$. Although DMRG is not applicable due to the nonlinearity of the Hamiltonian, gradient descent remains a viable optimization method. Gradient descent has been used to optimize an MPS when the tensors are isometry tensors [84–87]. In this work, we employ gradient descent within the MPS/QTT framework. The algorithm proceeds as follows. The QTT wavefunction is represented in canonical form, with one tensor at the orthogonality center—initially at the first site—and all tensors to the left (right) being left (right) orthogonal. The tensor at the orthogonality center is updated based on its energy gradient until it converges to a minimum. Once optimized, the orthogonality center is moved to the next site, and the process is repeated. This sweep continues back and forth until the global energy minimum is reached.

An essential step in the gradient descent method is to compute the energy gradient with respect to a tensor in the QTT wavefunction. The computational complexity is proportional to $dD^3D_W + d^2D^2D_W^2$. Again, we compute the gradients of the one-body energy $E^1[\psi]$ and the interaction energy $E_{\text{int}}[\psi]$ separately. Similarly to the ITE, the gradient of $E^1[\psi]$ can be computed straightforwardly with relatively low cost, but the exact computation for the gradient of $E_{\text{int}}[\psi]$ has complexity proportional to D^5 and is very slow (see Fig. 1(c)). To achieve efficient calculations, we compress $\psi^2(\mathbf{r})$ to a smaller bond dimension χ . The computation of the gradient $\partial_A E_{\text{int}}[\psi]$ is then reduced to a cost proportional to D^4 , which is the same as in the ITE.

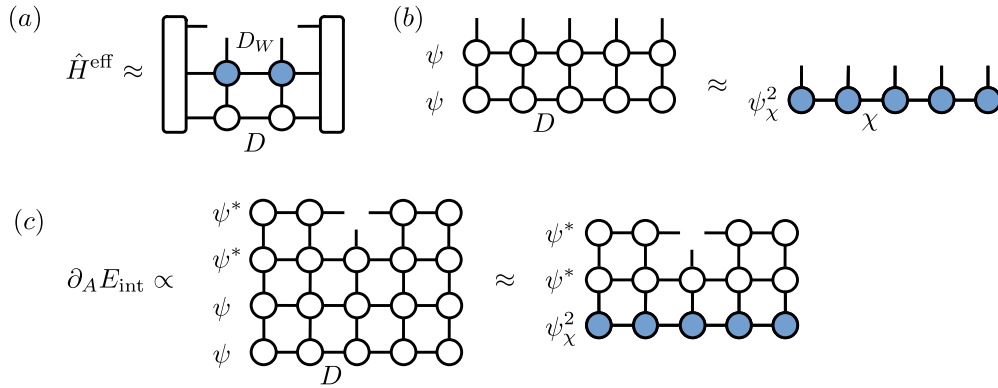


Figure 1: Schematic diagrams of tensor contractions and QTT structures. (a) The tensor contractions for computing the effective Hamiltonian. (b) QTT wavefunctions for ψ^2 and its compressed QTT form ψ_χ^2 . (c) Tensor contractions involved in computing the gradient of the interaction energy, shown for both the exact calculation and the approximation using ψ_χ^2 .

There is one thing we need to pay additional attention to in this approach. Since $\psi_\chi^2(\mathbf{r})$ is a single QTT that represents the product of wavefunctions $\psi^2(\mathbf{r})$, changing one tensor in $\psi(\mathbf{r})$ in

principle changes *all* the tensors in $\psi_\chi^2(\mathbf{r})$. This means that *all* the tensors in $\psi_\chi^2(\mathbf{r})$ needed to be recomputed for *each* update of a local tensor in $\psi(\mathbf{r})$, even in the internal loops of gradient descent. This significantly slows down the computations. Fortunately, in practice, we found that updating a few tensors around the orthogonality site in $\psi_\chi^2(\mathbf{r})$ is sufficient to achieve high accuracies for the gradient $\partial_A E_{\text{int}}[\psi]$ and for the slope along the descent direction. This is reasonable because in each update the tensor is changed only slightly, and the ‘‘correlation length’’ (regarding the qubits rather than the real space) is restricted by the bond dimension. Therefore, when the bond dimensions are small, changing a tensor in $\psi(\mathbf{r})$ corresponds to a ‘‘short-range’’ update for $\psi^2(\mathbf{r})$. As a demonstration, Fig. 2 shows the errors of the gradient $\partial_A E_{\text{int}}[\psi]$ and the slope along the descent direction, plotted as functions of the number of updating tensors in $\psi_\chi^2(\mathbf{r})$. The system is a BEC in a harmonic trap. It can be seen that the errors drop below 10^{-9} (10^{-14}) for the gradient (slope) when only three tensors are updated. In this work, we choose to update three tensors in $\psi_\chi^2(\mathbf{r})$ when a tensor in $\psi(\mathbf{r})$ is updated.

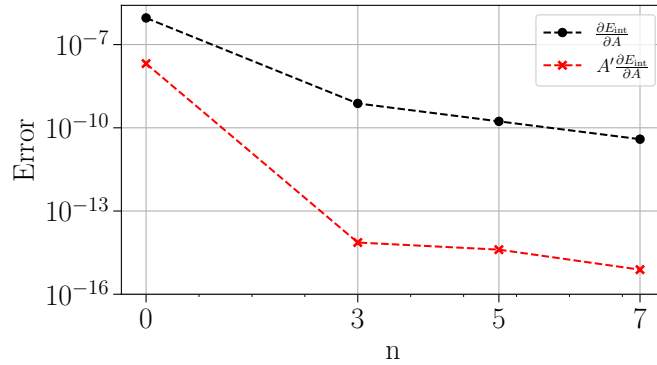


Figure 2: Absolute errors in the gradient of the interaction energy (black curve) and in the slope along the descent direction (red curve) as functions of the number of tensors updated in ψ_χ^2 after updating a tensor in ψ .

In this work, we employ the basic gradient descent method with line searches that satisfy the strong Wolfe conditions. While this approach is effective, more advanced optimization algorithms, such as quasi-Newton methods or the conjugate gradient descent method, can be used to further enhance convergence performance.

4 Benchmark

4.1 Two-dimensional BEC in a harmonic potential

We first benchmark our method on a system of a BEC in a harmonic trap. This corresponds to $\Omega = 0$ and $g = 100$ in the Hamiltonian in Eq. 4. The particle density of the ground-state wavefunction is shown in the inset of Fig. 3(a). This function can be efficiently represented in a QTT format with small bond dimensions. In Fig. 3(a), we show the errors of the QTT approximations with different bond dimensions D . The fidelity error is defined by $1 - |\langle \psi | \psi_{\text{QTT}} \rangle|^2$ where $|\psi\rangle$ is the exact ground state and $|\psi_{\text{QTT}}\rangle$ is the QTT wavefunction after compression. One can see that QTT achieves machine accuracy with error $\approx 10^{-16}$ with a bond dimension $D = 20$, and the error is not sensitive to the number of qubits. We thus choose $D = 20$ in the following benchmark.

To demonstrate the efficiency of QTT in terms of the number of grid points, we compare the computational time required for a single time-evolution step between the QTT method and the

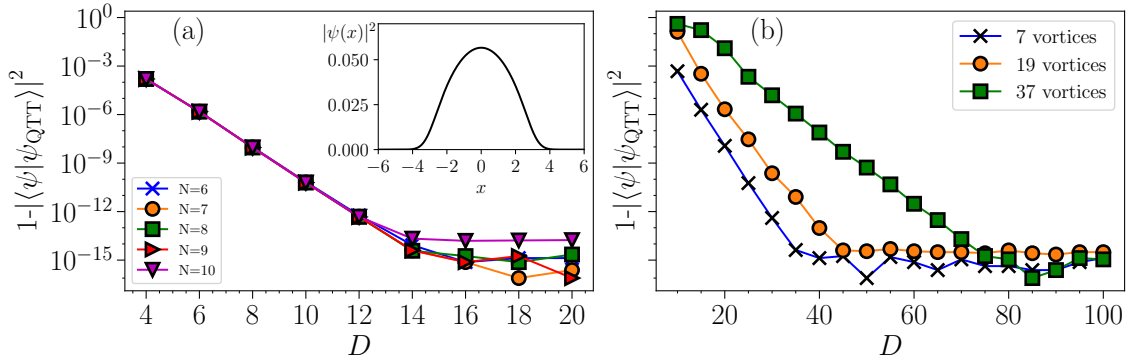


Figure 3: Absolute fidelity errors in the QTT of ground-state wavefunctions for (a) a BEC in a harmonic and (b) a BEC with vortices, plotted as functions of bond dimension D . The inset in panel (a) shows the density profile of the corresponding ground-state wavefunction. The density profiles of the vortex states can be found in Fig. 7.

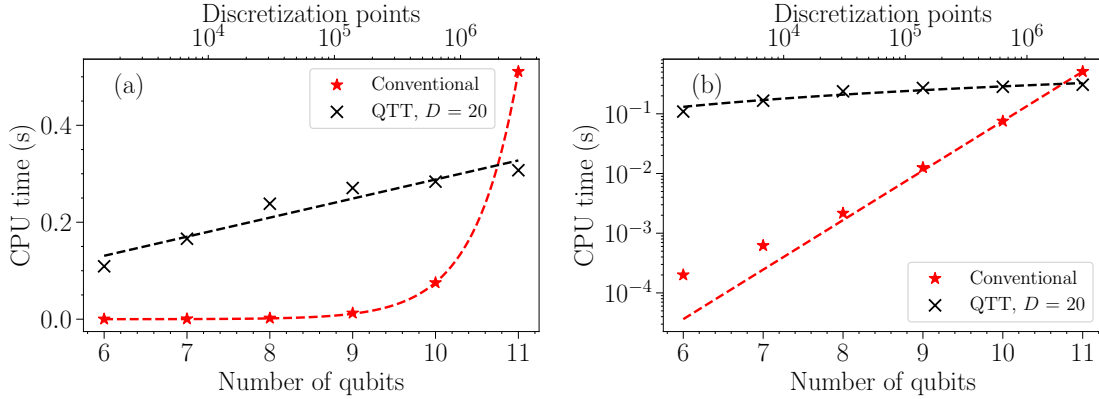


Figure 4: CPU times for a single ITE step using the QTT and conventional finite-difference methods, as functions of the number of qubits (equivalently, the number of grid points). Results are shown in (a) linear and (b) logarithmic scales to highlight the different scaling behaviors of the two approaches.

explicit ITE method with regular finite-difference discretization. In QTT formats, the number of grid points increases exponentially with the number of qubits, whereas the number of qubits increases linearly. This is directly reflected in the computational time: When the number of grid points increases exponentially, the QTT computational time scales only linearly, while the computational time for conventional discretizations grows exponentially, as shown in Fig. 4.

We then compare the efficiencies for the two ground-state algorithms, ITE and gradient descent. In Figs. 5(a) and (b), we show the errors of the chemical potential μ as functions of the CPU time and of the optimization steps for each method. Note that the variational method minimizes the energy $E[\psi]$ rather than the chemical potential μ . Therefore, μ is not variational and can be lower than the exact value during optimization. For ITE, an optimization step is defined by an evolution of a time step $\delta\tau$, and for the variational method, an optimization is defined by a complete sweep of optimizations. Both methods obtain μ with an accuracy up to 10^{-10} with bond dimension $D = 20$, showing excellent representations of the ground state. Although the ITE is slightly faster at each optimization step, gradient descent is overall more efficient because it converges much faster in each iteration. For a fixed D , the errors saturate in a large number of optimization steps because the bond dimension D limits the accuracy of

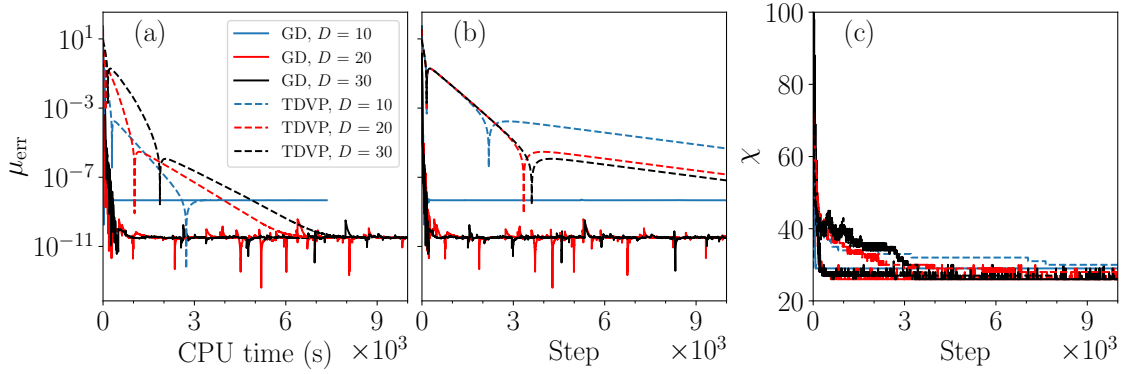


Figure 5: Convergence of the chemical potential μ computed using gradient descent (GD) and TDVP within the QTT framework, shown as functions of (a) CPU time and (b) optimization steps, for a BEC in a harmonic trap. Different colors correspond to different bond dimensions of the QTT wavefunctions. Panel (c) shows the evolution of the bond dimension of $\psi_\chi^2(\mathbf{r})$ during the optimization.

$\psi(\mathbf{r})$. One can systematically improve the accuracy by increasing the bond dimension D .

As mentioned in Sec. 3, the computational cost significantly depends on the efficiency of compressing $\psi^2(\mathbf{r})$ to a smaller bond dimension χ . In Fig. 5(c), we show the behaviors of χ as functions of optimization steps, given the truncation cutoff $\epsilon_{\psi^2} = 10^{-12}$. It can be seen that, for both ITE and GD, χ starts from rather large initial values (but still much smaller than D^2) in the early stages of the simulations, and eventually converges to values close to D . This can be understood because in the early stages of the simulations, the variational wavefunctions are far from the ground state and can lead to rather complicated structures in $\psi_\chi^2(\mathbf{r})$. When the wavefunction approaches the ground state, which is typically smooth, $\psi_\chi^2(\mathbf{r})$ has similar structures to $\psi(\mathbf{r})$ and the bond dimension χ saturates to a value in the same order as D .

4.2 Rotating BEC

We then consider a more challenging system, a BEC in a rotating frame with angular frequency Ω . The system will induce vortices as the lowest-energy excitations, which form a triangular lattice. The number of vortices depends on the angular momentum Ω and the system size [77, 82], which can be estimated by

$$N_v \approx \frac{m\Omega}{\pi\hbar} \pi R_{\text{TF}}^2 \quad (10)$$

where $R_{\text{TF}} = [4gN_c/\pi m(\omega^2 - \Omega^2)]^{1/4}$ with the condensate number N_c ² is the Thomas-Fermi radius of the system. Noting that this estimation ignores the effect of the density inhomogeneity, and hence is only a crude prediction.

Fig. 3(b) shows the errors of QTT compressions for the ground states versus the bond dimension D for different numbers of vortices and with the number of qubits $N_{\text{qub}} = 8$ (corresponding to 256 grid points) for each dimension. Compared to the system without a vortex, the wavefunctions require larger bond dimensions to achieve high accuracy, and the required bond dimensions depend on the number of vortices.

To benchmark the efficiency of the methods, we first focus on a Hamiltonian with $\Omega = 0.8$ and $g = 100$, where the ground state has 7 vortices. The vortex pattern for the ground state

²In the dimensionless form in this work, see Appendix A for detail, the dimensionless Thomas-Fermi radius is $R_{\text{TF}} = [4g/\pi(\omega - \Omega^2)]$ where g is dimensionless and account the contribution of N_c according the normalization condition.

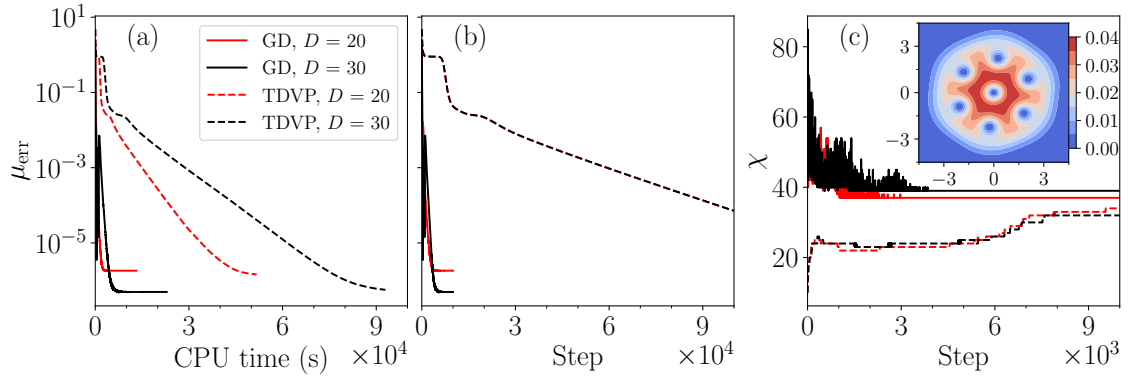


Figure 6: Convergence of the chemical potential μ computed using gradient descent (GD) and TDVP within the QTT framework, as functions of (a) CPU time and (b) optimization steps, for a BEC ground state containing 7 vortices. Different colors indicate different bond dimensions of the QTT wavefunction. Panel (c) shows the evolution of the bond dimension of $\psi_\chi^2(\mathbf{r})$ during optimization. The inset displays the corresponding density profile in domain $[-6, 6]^2$ with $N_{\text{qub}} = 8$.

is shown in the inset of Fig. 6(c), showing a clear triangular lattice. We compare the computational efficiencies of the two QTT ground-state methods. Fig. 6(a)(b) shows the errors of chemical potential μ as functions of the CPU time and of the optimization steps. Similarly, the errors obtained from gradient descent decrease significantly faster than those obtained from ITE, showing the outperformance of gradient descent over ITE. The accuracies can be systematically improved by increasing the bond dimensions D . During gradient descent optimization, the bond dimensions χ of the compressed wavefunction square $\psi_\chi^2(\mathbf{r})$ start from relatively large values, and gradually decrease, eventually saturating to values on the same order as D , given a truncation cutoff of $\epsilon_{\psi^2} = 10^{-8}$, as shown in Fig. 6(c). In the ITE, in contrast, the bond dimension χ initially has lower values, then increases, and eventually saturates to the same order as D during the evolution.

To demonstrate the power of the QTT approach, we then consider more challenging systems with larger Ω , where the numbers of vortices in the ground states range from 19 to 125, on a dense $2^{17} \times 2^{17}$ meshgrid. We obtain well-converged wavefunctions that show clear triangular lattices in all cases. Their densities of the wavefunctions are shown in Fig. 7(a)-(f). We emphasize that for large values of Ω , the vortex number can be sensitive to the spatial resolution, making it important to approach the fine-grid limit. We demonstrate the grid-resolution effect in Sec. D.3.

In practice, using the converged wavefunction with fewer vortices as the initial state significantly improves convergence when computing ground states with a larger number of vortices. It is also helpful to start from a QTT representation with fewer qubits and gradually increase the number of qubits using linear interpolation. The corresponding Hamiltonian parameters and the bond dimensions of $\psi(\mathbf{r})$ are summarized in Tab. 1.

We benchmark the efficiency of our method on a system with 19 vortices (Fig.7(b)) on a $2^{11} \times 2^{11}$ meshgrids against several conventional methods with regular discretization, including the backward Euler pseudo-spectral method (BESP) [54], the backward Euler finite-difference method (BEFD) [54], and the explicit ITE method. The initial state is chosen to be a 7-vortex state for all methods. In Fig. 8, we compare the errors in chemical potential μ and the total energy E as functions of CPU time from different methods. Clearly, the QTT gradient descent method outperforms all the conventional methods, due to the high efficiency of compressing the wavefunctions in QTT structures. More details of the benchmark results are shown in

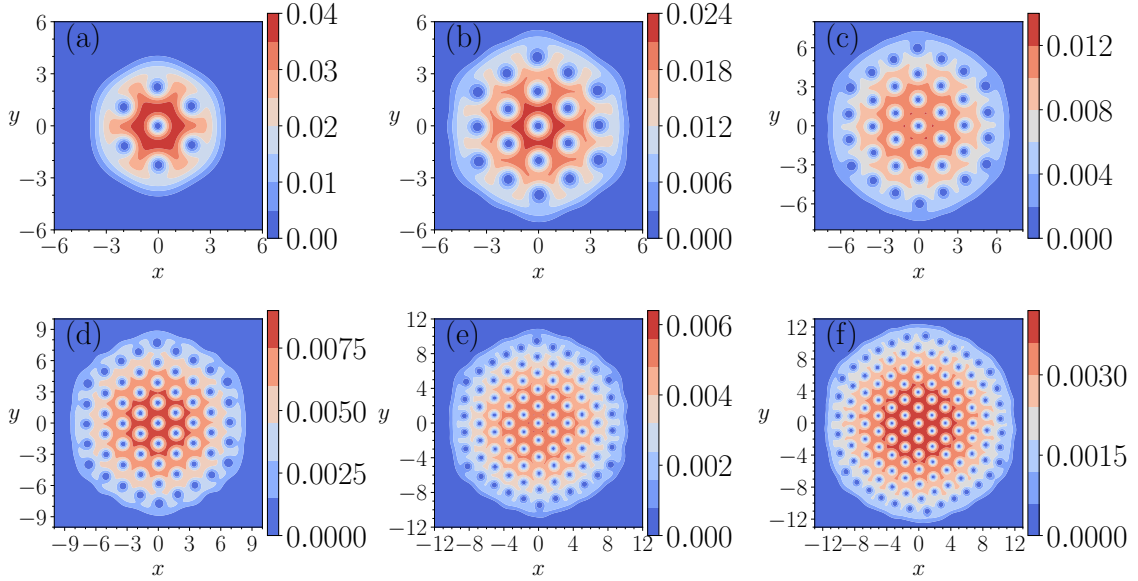


Figure 7: Density profiles of the ground states containing (a) 7, (b) 19, (c) 37, (d) 61, (e) 91, and (f) 125 vortices. All simulations are performed on a domain of $[-21, 21]^2$ using $2^{17} \times 2^{17}$ grid points. The physical parameters, as well as the corresponding energies and chemical potentials of each system, are listed in Tab. 1.

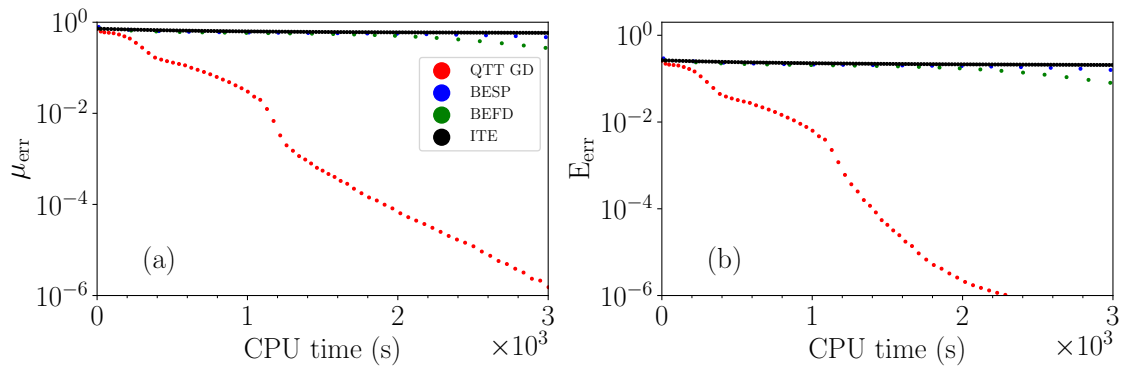


Figure 8: The CPU time of the QTT gradient descent method is compared with several conventional methods, including BESP, BEFD, and the ITE method. Each point in the figure corresponds to 20 iterations. The system contains 19 vortices, and all simulations start from the same initial state with 7 vortices. The computational domain is $[-21, 21]^2$, and the number of grid points is $2^{11} \times 2^{11}$.

Number of vortices	Ω	g	D	N_{qub}	μ	E
7	0.8	100	30	17	4.35	3.19
19	0.946	100	30	17	2.90	2.25
37	0.913	500	40	17	6.36	4.54
61	0.9616	500	50	17	4.67	3.42
91	0.9617	1100	65	17	6.46	4.59
125	0.972	1550	80	17	6.63	4.68

Table 1: Hamiltonian parameters Ω and g , the bond dimension D , and the number of qubits N_{qub} per dimension for the QTT ground states with different numbers of vortices shown in Fig. 7. The chemical potential μ and total energy E are evaluated using the gradient descent algorithm.

Sec. D.2.) We emphasize that we choose the grid resolutions to keep the computational time manageable for the conventional methods. The advantage of the QTT method over conventional methods is expected to be even more pronounced on finer grids.

4.3 Dynamics

The real-time evolution of a QTT wavefunction can be performed using the same TDVP algorithm employed for the ground state. Here, we consider the time evolution of a BEC in a harmonic trap ($\Omega = 0$) after a sudden quench from an initial interaction strength $g_1 \approx 12.5$ to a smaller value $g_2 = g_1/2$. After the quench, the system behaves in a so-called *breathing mode* where the width of the wavefunction oscillates in time with frequency 2ω [77, 88, 89], where ω is the harmonic trap frequency defined in the Hamiltonian in Eq. 4. Fig. 9(a) shows the wavefunction width as a function of time for two different truncation cutoffs ϵ . In both cases, the results perfectly agree with the expected oscillation frequency.

In these simulations, both the bond dimensions of $\psi(\mathbf{r})$ and $\psi^2(\mathbf{r})$ are controlled by the same cutoff ϵ , and can in principle grow in time. However, there is an essential difference between the evolution of QTT wavefunctions and many-body MPS wavefunctions. For evolutions of many-body states, the MPS bond dimensions typically grow exponentially over time due to the growth of entanglement, which limits the accessible time. In contrast, the bond dimension of a QTT depends on the smoothness and the correlations between different scales of the wavefunction. If the wavefunction remains smooth during the evolution, a QTT wavefunction may have a small bond dimension for an arbitrary long time. In the systems we consider, the wavefunction remains smooth and simple throughout the entire evolution, allowing for efficient simulations over arbitrarily long times. In Fig. 9(b), we show that the bond dimensions of $\psi(\mathbf{r})$ and $\psi^2(\mathbf{r})$ as functions of time with truncation cutoff $\epsilon = 10^{-8}$. They stay with small values and do not grow over the entire simulation. These results indicate that the QTT framework is a promising approach for simulating the dynamics governed by the GPE.

5 Conclusion and Discussion

We have introduced an efficient and scalable computational framework based on the QTT format for solving the GPE, which models BECs within the mean-field approximation. By extending tensor network techniques, we adapted the ITE and developed a gradient-based variational method to handle the nonlinear interaction term. A key element of our approach is the compression of the nonlinear term into a compact QTT representation, which greatly reduces computational complexity without compromising accuracy. This allows for the simu-

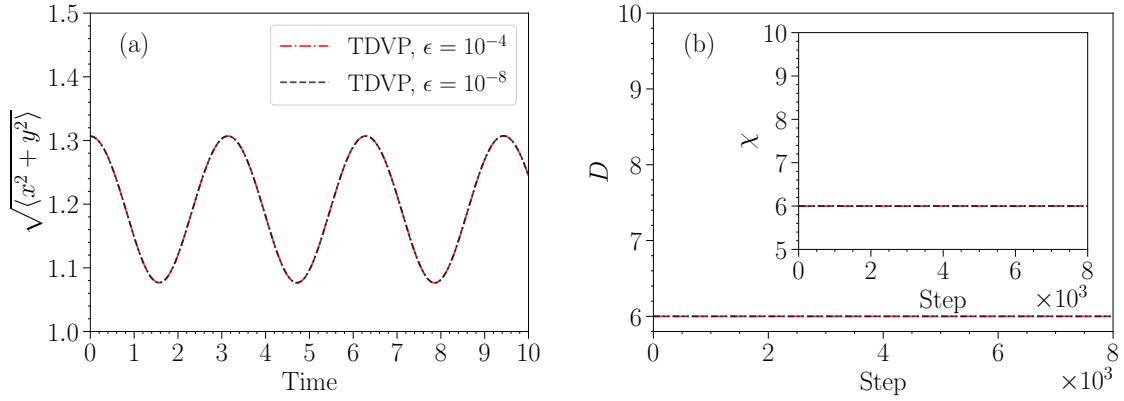


Figure 9: (a) Time evolution of the wavefunction width in the breathing mode simulated using TDVP with two different truncation cutoffs ϵ . (b) Bond dimensions D of $\psi(\mathbf{r})$ and χ of $\psi_\chi^2(\mathbf{r})$ as functions of optimization step for the corresponding truncation cutoffs.

lation of large, highly resolved systems that are otherwise difficult to treat with conventional grid-based methods.

We demonstrated that QTT-based methods outperform conventional approaches in both accuracy and efficiency, particularly as the system size and resolution increase. For ground-state calculations, the gradient descent algorithm converges more rapidly and achieves better numerical performance than imaginary-time evolution. In rotating condensates, we computed vortex lattice ground states with up to several dozen vortices using modest computational resources. These wavefunctions can be efficiently compressed in QTT representations with small bond dimensions, allowing efficient computations even in the fine-grid limit. This calculation provides a path forward for large-scale simulations in mean-field quantum systems, such as the superfluids in neutron stars, where 10^{18} - 10^{20} vortex lines with femtometre-scale core size are expected within a 100km^2 area of a neutron star's interior [63, 74]. For real-time dynamics, we showed that the bond dimension remains stable over long simulation times, enabling efficient and accurate simulations of nonlinear quantum evolution.

We also note that the QTT framework targets a specific type of approximation and, in principle, can be combined with existing methods, for example, adaptive meshes or implicit time-integration methods. Such combinations would allow approaches that benefit from both techniques. Therefore, QTT should not be viewed simply as competing with other methods, but rather as an alternative approach that can be effectively integrated with them.

Overall, our results establish the QTT framework as a powerful tool for solving nonlinear quantum equations. By combining high compression efficiency with algorithmic flexibility, it provides a path forward for large-scale simulations in mean-field quantum systems and offers new opportunities for applying tensor network methods to nonlinear and continuum problems in physics.

Acknowledgements

We acknowledge helpful discussions with X. Waintal. Chia-Min Chung thanks the CTCR, NYCU, Taiwan, for providing full support.

Funding information C.-M. C. acknowledges support by MOST (111-2112-M-110-006-MY3, 113-2112-M-110-026, and 114-2628-M-110-005-MY3) and the Yushan Young Scholar Program under the Ministry of Education (MOE) in Taiwan. I.-K. Liu is supported the Science and Technology Facilities Council (ST/W001020/1). J.-W. L. acknowledges funding support from the Plan France 2030 ANR-22-PETQ-0007 “EPIQ”

A Normalization

The normalization consistency between continuum and discrete representations poses a fundamental challenge in quantum tensor train (QTT) simulations. Consider the 2D Gross-Pitaevskii equation (GPE) chemical potential formulation:

$$\mu_{2D} = \sum_{i,j} \psi^*(\mathbf{r}_{ij}) \left[-\frac{1}{2} \nabla_{i,j}^2 + \frac{1}{2} \omega^2 \mathbf{r}_{ij}^2 + g |\psi(\mathbf{r}_{ij})|^2 - \Omega L_z \right] \psi(\mathbf{r}_{ij}) \Delta x \Delta y, \quad (11)$$

where $\mathbf{r}_{ij} = (x_i, y_j)$ denotes discrete grid coordinates with uniform spacing $\Delta x = \Delta y$. The normalization condition enforces:

$$\sum_{i,j} |\psi(\mathbf{r}_{ij})|^2 \Delta x \Delta y = 1. \quad (12)$$

For the QTT canonical form, we introduce dimensionless wavefunction $\tilde{\psi}$ through the transformation:

$$\tilde{\psi}(\mathbf{r}_{ij}) = \psi(\mathbf{r}_{ij}) \Delta x, \quad (13)$$

yielding modified normalization:

$$\sum_{i,j} |\tilde{\psi}(\mathbf{r}_{ij})|^2 = 1. \quad (14)$$

The Hamiltonian undergoes corresponding rescaling:

$$\hat{H}[\tilde{\psi}] = -\frac{1}{2} \nabla^2 + \frac{1}{2} \omega^2 r^2 + \frac{g}{(\Delta x)^2} |\tilde{\psi}|^2 - \Omega L_z. \quad (15)$$

The QTT chemical potential calculation preserves continuum values through careful dimensional analysis:

$$\tilde{\mu}_{2D} = \sum_{i,j} \tilde{\psi}^*(\mathbf{r}_{ij}) \hat{H}[\tilde{\psi}] \tilde{\psi}(\mathbf{r}_{ij}) = \sum_{i,j} \psi^*(\mathbf{r}_{ij}) \Delta x [\hat{H}[\psi]] \psi(\mathbf{r}_{ij}) \Delta x = \mu_{2D},$$

then, the rescaled nonlinear coupling parameter exhibits critical scaling behavior:

$$g' = \frac{g}{(\Delta x)^2}. \quad (16)$$

For typical parameters $\Delta x < 10^{-8}$ and $g > 10^2$, we observe:

$$g' > 10^{18} \quad (2D \text{ case}), \quad g' > 10^{26} \quad (3D \text{ case}). \quad (17)$$

This divergence imposes severe numerical stability constraints, particularly in higher dimensions where the scaling becomes $g' \propto (\Delta x)^{-d}$ for spatial dimension d .

B Review of Quantic Tensor Train

In this section, we review the basic concepts of the quantic tensor train (QTT) used in this work. We explain how a function can be represented in the QTT format and how operators are expressed as QTT operators (QTTO).

From function to tensor. Since QTT is a decomposition method for multi-index tensors, it is helpful to first clarify how a function can be represented as an N -index tensor. For simplicity, consider a one-dimensional function $f(x)$ defined on a discretized grid with 2^N points $\{x_i\}$, where $i = 1, 2, \dots, 2^N$. Each index i can be represented by an N -bit binary number: $\{b_1 b_2 \dots b_N\}$, with $b_j \in \{0, 1\}$. For example, $i = 1$ corresponds to $\{00 \dots 00\}$, $i = 2$ to $\{10 \dots 00\}$, and so forth. Each bit b_j is often referred to as a *qubit*, highlighting the conceptual link to quantum computing. The discretized function values $f(x_i)$ can thus be relabeled as $f_{b_1 b_2 \dots b_N}$, forming an N -index tensor, as illustrated in Fig. 10(a). This relabeling is exact and does not involve approximation; the tensor retains all 2^N original function values. In graphical tensor notation, this representation is illustrated in Fig. 10(b), where each open leg represents a qubit index. Once in this form, the tensor can be decomposed into the QTT format.

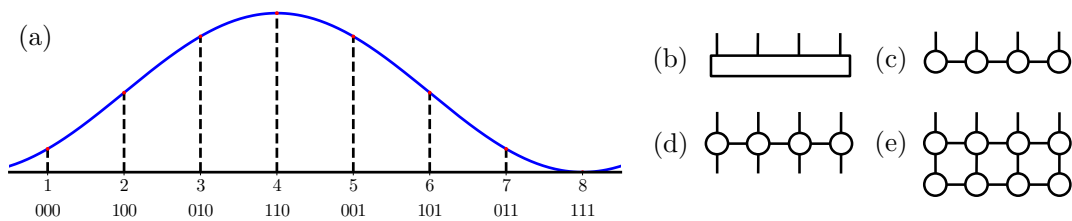


Figure 10: (a) TT/MPS representation of a 4-index tensor. The open legs represent the qubits/physical indices, and the shared legs represent the virtual indices. (b) An MPO (or tensor train operator) that represents an operator, for example $\frac{d^2}{dx^2}$. (c) MPO-MPS contraction, which computes the application of an operator to a function, for example $\frac{d^2}{dx^2}f$, or a product of two function $f \cdot g$.

TT/MPS decomposition. The QTT decomposition represents an N -index tensor as a chain of N smaller tensors connected through internal indices known as *bond dimensions*, as shown in Fig. 10(c). Smooth functions typically have low correlations across different scales, allowing the tensor to be compressed efficiently into a QTT form with small bond dimensions. For certain functions, exact QTT decompositions are known (see Appendix C for examples). In general, however, one must numerically determine the QTT representation using techniques such as *tensor cross interpolation* (TCI) [90–94]. TCI is a powerful algorithm that learns QTT tensors from sampled values of the target function, controlling the bond dimensions and thus the accuracy of the approximation.

For functions of two or higher dimensions, the representation can be generalized straightforwardly by assigning N qubits to each spatial dimension. In this work, we specifically focus on two-dimensional wavefunctions. We use the so-called *mirror ordering*, placing qubits representing large-scale structures at the center of the QTT chain and those corresponding to small-scale details at the edges.

The computational cost grows linearly with the total number of qubits, making simulations at exponentially fine discretization straightforward. The main computational challenge typically arises from the bond dimensions, which strongly depend on the structure of the target functions and thus vary across different systems.

Operator representation as QTTO. Similar to the representation of functions in QTT format, physical operators can be represented in the QTT framework as matrix product operators (MPOs) by doubling the number of qubits, as illustrated in Fig. 10(d). In this work, we focus

mainly on the Laplacian operator ∇^2 , which appears naturally in terms of kinetic energy. An exact MPO representation for this operator is given explicitly in the Supplementary Material.

Function operations in QTT format. Operations such as the product or addition of two functions can be performed directly in the QTT format. To calculate a product $f(x)g(x)$, it is often convenient to represent one of the functions (e.g., $f(x)$) as a QTTO. Specifically, starting from the QTT form of the function $f(x)$, each tensor's qubit index is duplicated into a diagonal form, transforming a QTT tensor $A_{\alpha_i \beta_i}^{b_i}$ into an MPO-type tensor $A_{\alpha_i \beta_i}^{b_i b'_i} = A_{\alpha_i \beta_i}^{b_i} \delta_{b_i b'_i}$, where b_i denotes the qubit index and α_i, β_i represent the left and right bond indices, respectively. With $f(x)$ now in QTTO form, the product $f(x)g(x)$ can be computed efficiently through an MPO-MPS contraction, as depicted in Fig. 10(e).

Similarly, the addition of two functions or operators can be efficiently implemented using standard methods for adding MPSs or MPOs [2]. Using this approach, complex operators can be constructed directly from simpler, elementary operators. For example, the angular momentum operator $\hat{L}_z = \hat{x}\hat{p}_y - \hat{y}\hat{p}_x$ can be built from basic operators \hat{x} , \hat{y} , \hat{p}_x , and \hat{p}_y , each of which has an exact QTTO representation.

C Exact QTT representations

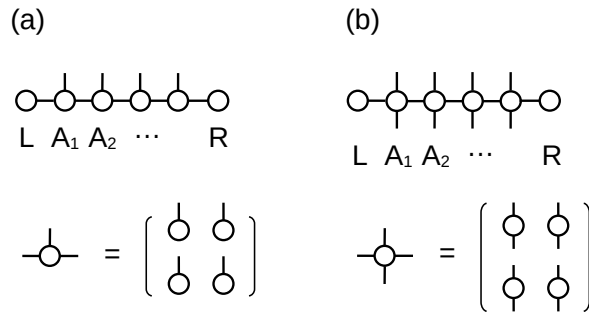


Figure 11: The representations of tensors as (a) a matrix of vectors for a QTT, and (b) a matrix of matrices for an MPO. The corresponding indices for the elements are shown in the lower panels.

Here we introduce some functions and operators that have the exact QTT representations. To represent the tensors, we write the tensors in matrix form, where each element is a vector (matrix) for a function (operator). The corresponding indices are sketched in Fig. 11(a-b).

Linear functions. A linear function $f(x) = ax + b$ can be represented in the QTT form efficiently. It is convenient to first consider $f(x) \rightarrow f_{b_1 b_2 \dots b_N} = x_{\text{Int}}$ for integer x_{Int} from 0 to $2^N - 1$. The QTT representation for $f_{b_1 b_2 \dots b_N}$ can be easily obtained from the binary representation of integers, $x_{\text{Int}} = \sum_{i=1}^N b_i 2^{i-1}$, where $b_i = \{0, 1\}$ are the qubit degrees of freedom and N is the number of qubits. The QTT tensor on site i is thus

$$A(i) = \begin{pmatrix} \mathbf{I} & \mathbf{0} \\ \mathbf{t}_i & \mathbf{I} \end{pmatrix}, \quad \mathbf{I} = \begin{pmatrix} 1 \\ 1 \end{pmatrix}, \quad \mathbf{t}_i = \begin{pmatrix} 0 \\ 2^{i-1} \end{pmatrix} \quad (18)$$

– each \mathbf{t}_i contributes 0 or 2^i to x depending on b_i . The product of the tensors accumulate the sum of \mathbf{t}_i to the corner,

$$\prod_i A(i) = \begin{pmatrix} \mathbf{I} & \mathbf{0} \\ \sum_i \mathbf{t}_i & \mathbf{I} \end{pmatrix}. \quad (19)$$

The left and the right edge tensors are defined as

$$L = \begin{pmatrix} 0 & 1 \end{pmatrix}, \quad R = \begin{pmatrix} 1 \\ 0 \end{pmatrix}. \quad (20)$$

to pick up the corner element $\sum_i \mathbf{t}_i$ from $\prod_i A(i)$.

To represent $f(x) = x$ in an arbitrary range between x_i and x_f with N qubits (corresponding to 2^N discretization points), one can rescale and translate the integer x_{int} to the desired range. More precisely, $f(x) = x = \alpha x_{\text{int}} + \beta$ where $\alpha = \frac{x_f - x_i}{2^N}$ and $\beta = x_i$. This can be done by defining L as

$$L = \begin{pmatrix} \beta & \alpha \end{pmatrix}. \quad (21)$$

A general linear function $f(x) = ax + b$ in a range between x_i and x_f can be obtained by using $\alpha = a \frac{x_f - x_i}{2^N}$ and $\beta = b + x_i$.

Polynomial functions. A polynomial function can be obtained by using product and addition from $f(x) = x$. The product and the addition can be achieved with the standard MPS algorithms.

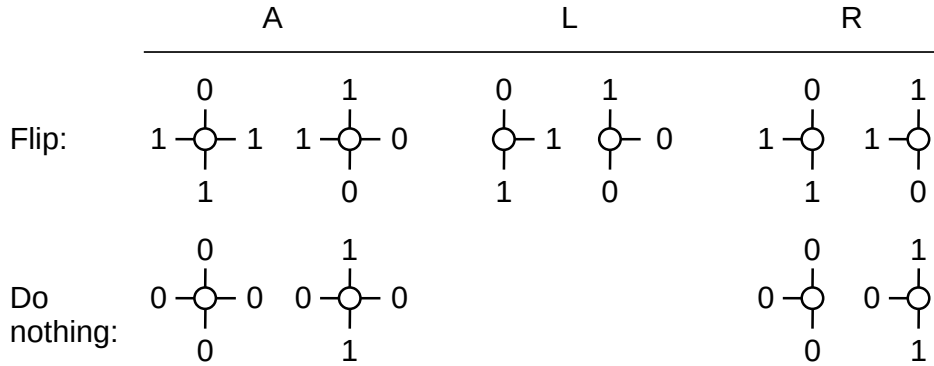


Figure 12: The non-zero elements in the tensors A , L and R for the operator $\frac{d}{dx}$. The numbers indicate the labels for the non-zero elements. These elements have values equal to one.

Differential operators The most important operator for us is the Laplace operator ∇^2 which allows us to define the kinetic energy operator. To obtain the MPO form of ∇^2 , we first consider a one-dimensional differential operator $\frac{d}{dx}$. The higher dimensional operators can be obtained straightforwardly by extending the number of qubits. In the discrete space, $\frac{d}{dx} \rightarrow \frac{1}{\Delta x} [\hat{T}(\Delta x) - \hat{I}]$ where $\hat{T}(\Delta x)$ is the translational operator for a smallest distance Δx in the discretized space, and \hat{I} is the identity operator. The task is to find out $\hat{T}(\Delta x)$ defined by $\hat{T}(\Delta x)f(x) = f(x + \Delta x)$, which is nothing but an "plus one" operator for binary numbers. For example, $\hat{T}(\Delta x)$ maps a binary number 1100 from the lower qubits to 0010 from the upper

qubits. Note that to be consistent with the programming language, we consider the smallest scale represented by the leftmost qubit. The logic of this operator can be summarized as follows. For each qubit,

1. if all the qubits from the left are 1, flip the qubit from 0 to 1 or from 1 to 0;
2. otherwise, do nothing.

This operation can be encoded in an MPO tensor with bond dimension 2, where the left index j is used to indicate the above two conditions:

1. $j = 1$: All the qubits from the left are 1
2. $j = 0$: Otherwise

As a result, the tensor has only 4 non-zero elements with value 1, as shown in Fig.12, which can be concluded by the following tensor

$$A = \begin{pmatrix} \hat{I} & \hat{\sigma}^+ \\ \hat{\sigma}^+ & \hat{\sigma}^- \end{pmatrix} \quad (22)$$

where \hat{I} is the identical matrix, and $\hat{\sigma}^+$ and $\hat{\sigma}^-$ are the raising and lowering operators. The rightmost qubit follows the same rules so the tensor is the same except no right index is needed. The leftmost qubit (first digit) should always flip. Therefore the left and the right edge tensors are defined as

$$L = \begin{pmatrix} 0 & 1 \end{pmatrix}, \quad R = \begin{pmatrix} 1 \\ 1 \end{pmatrix}. \quad (23)$$

Note that in this definition, the derivative of the last point $11 \cdots 1$ is defined by the last point $11 \cdots 1$ and the first point $00 \cdots 0$. In this sense, the wavefunction has periodic boundary condition.

D Convergence behavior

D.1 BEC in a harmonic trap

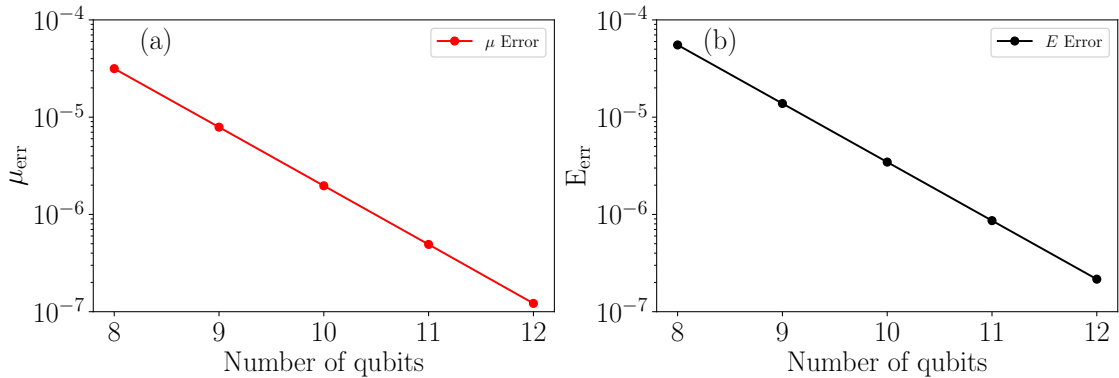


Figure 13: Absolute errors in the chemical potential (a) and total energy (b) as functions of the number of qubits for each dimension for a system of a BEC in a harmonic trap.

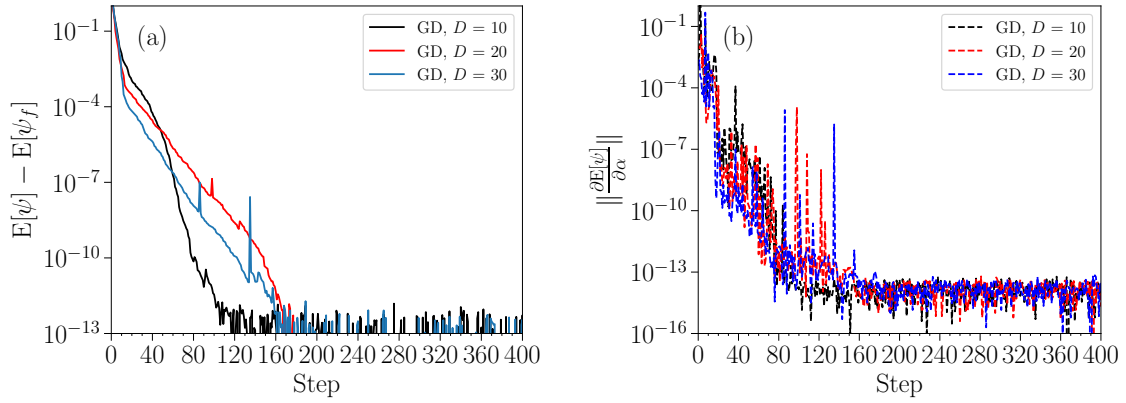


Figure 14: (a): In the GD method, the value of the variational functional $E[\psi]$ should strictly decrease with the number of steps in the early steps (Step < 30). As the functional value converges to the precision of the MPS and MPO themselves (ϵ : cutoff), the functional value starts to exhibit noise (Step > 50). E_{ψ_f} is the functional value at the last step. (b): It is the derivative of E with respect to step length α . For the GD algorithm, determining whether ψ has converged means checking if $\frac{\partial E_{\psi}}{\partial \alpha}$ is zero or it has reached machine precision.

In this section, we discuss the convergence properties of QTT methods in more detail. We demonstrate on a system of a BEC in a harmonic trap (see Fig. 3(a)). We first show the absolute errors of chemical potential μ and energy E as functions of the number of qubits for each dimension in Fig. 13. (The number of grid points grows exponentially with the number of qubits.) As expected, the errors decay exponentially with the number of qubits, showing the efficiency of the QTT approach.

We then discuss the convergence properties in the variational method. In the variational method, we minimize the energy $E[\psi]$ rather than the chemical potential μ . Therefore, μ can be lower than the exact value during the optimizations. In Fig. 14(a), we show the convergence of the energy for the system of BEC in a harmonic trap. It can be seen that the energy decreases almost monotonically and is always higher than the exact value during the optimization steps. In some steps, the energy jumps up and then decreases again. This is because the gradient in our method is computed approximately and could sometimes allow an increase in energy. However, this does not slow down the overall convergence in the algorithm. In Fig. 14(b), we show the energy slopes along the searching directions as functions of optimization steps. Similar to the energies, the slopes decrease rapidly to almost zero with optimization steps, showing convergence of the simulations.

D.2 Vortex systems

In this section, we provide more details on the benchmark comparing the QTT method with conventional methods, including BESF, BEFD, and ITE, to complement the discussion corresponding to Fig. 8 in the main text. In Fig. 15 (a-d), we show the data from the same simulation as in Fig. 8, but with longer iterations. Each data point corresponds to ? iterations. In Fig. 15 (e-h), we show the density profile after performing 800 iterations in each method. It can be seen that the QTT method efficiency clearly outperforms the conventional methods in both the number of iterations and CPU time. We note that we use a variational method in QTT, while all the conventional methods here are based on imaginary-time evolutions. However, we argue that the main advantage of the QTT method lies in its high efficiency in compress-

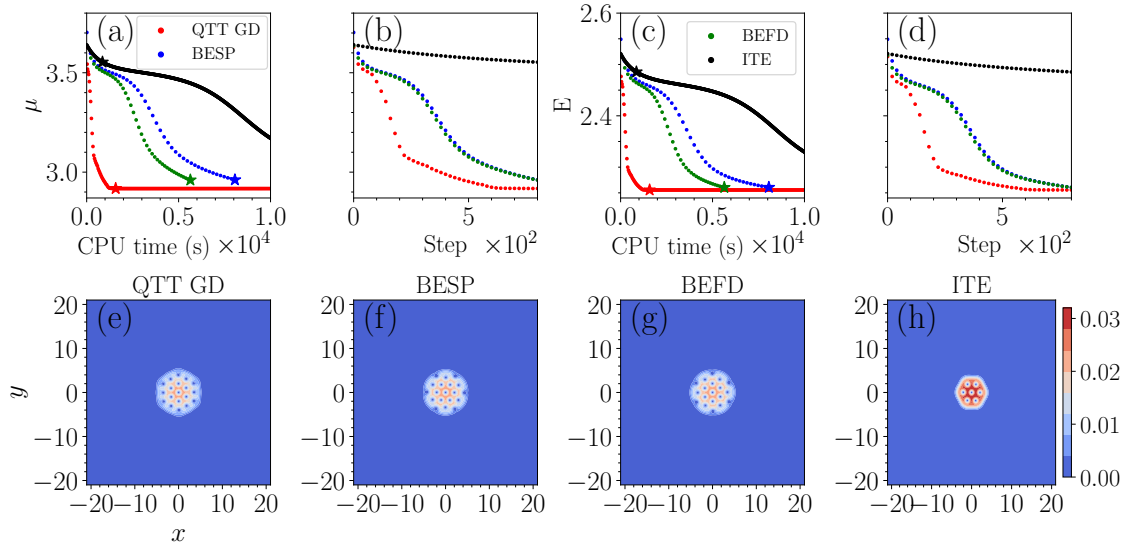


Figure 15: (a–d) Comparisons of convergence behaviors for chemical potential μ and energy E versus CPU time and the number of iteration steps for the QTT-GD method and conventional methods (BESP, BEFD, and ITE), complementing Fig. 8. The simulations are performed on a domain of $[-21, 21]^2$ using $2^{11} \times 2^{11}$ grid points. Each point corresponds to $[\cdot]$ iterations in each algorithm. The stars in (a) and (c) indicate the state at 800 iterations. (e–h) Wavefunction densities after 800 iterations for each method.

ing the wavefunction on a high-resolution mesh. The optimization algorithms (variational or imaginary-time evolution) do not play a significant role in the performance in these comparisons.

The parameters we used for the conventional methods are summarized as follows. For ITE, we use $dt = 0.00021$ to fulfill the CFL condition. For BEFD and BEST, since they are back Euler method, we use $dt = 0.01$. For BEFD and BESP, the convergence criteria for the Krylov space residue are 10^{-9} or 10^3 iteration number, and the normalized norm error is set to be 10^{-4} . Benchmark comparisons in Fig. 8 and Fig. 15 were performed on an AMD Ryzen™ 9 9950X3D CPU with 128 GB RAM (KF556C36-32, 32 GB \times 4), running Ubuntu 24.04.3 LTS and MATLAB R2025b Update 1.

D.3 Effect of meshgrid resolution

For systems containing a large number of vortices, grid resolution becomes important to obtain the correct wavefunctions. To demonstrate the effect of grid resolution, we start from a converged wavefunction, as shown in Fig. 7(f), which contains 125 vortices on a $[2^{17} \times 2^{17}]$ grid, and then reduce to lower resolutions by averaging the fine scales. We then use these lower-resolution wavefunctions as initial states to variationally find the ground states of the *same* system at different resolutions. Note that the initial wavefunctions for all the resolutions contain 125 vortices, which is the right number of vortices in the continuous limit. However, after optimization, different resolutions end up converging to wavefunctions with different numbers of vortices, as shown in Fig. 16. It shows that for a complicated system, it is important to use a grid with fine enough resolution to obtain the correct wavefunction. This highlights the importance of QTT-based methods, which enable us to achieve high-resolution grids with minimal effort.

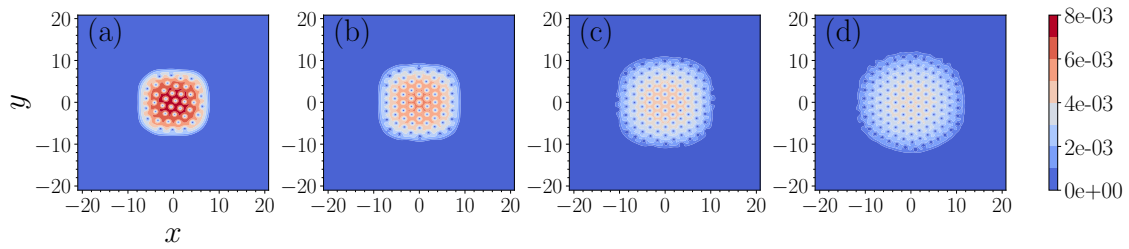


Figure 16: Density distributions obtained from the wave function of Fig. 7(f) after compression to different mesh grids and evolution for 2000 time steps with fixed parameters g , Ω , and $D = 80$: (a) $2^8 \times 2^8$, (b) $2^9 \times 2^9$, (c) $2^9 \times 2^9$, (d) $2^{11} \times 2^{11}$.

References

- [1] I. P. McCulloch, *From density-matrix renormalization group to matrix product states*, Journal of Statistical Mechanics: Theory and Experiment **2007**(10), P10014 (2007), doi:[10.1088/1742-5468/2007/10/P10014](https://doi.org/10.1088/1742-5468/2007/10/P10014).
- [2] U. Schollwöck, *The density-matrix renormalization group in the age of matrix product states*, Annals of Physics **326**(1), 96 (2011), doi:<https://doi.org/10.1016/j.aop.2010.09.012>, January 2011 Special Issue.
- [3] S. R. White, *Density-matrix algorithms for quantum renormalization groups*, Phys. Rev. B **48**, 10345 (1993), doi:[10.1103/PhysRevB.48.10345](https://doi.org/10.1103/PhysRevB.48.10345).
- [4] S. R. White, *Density matrix formulation for quantum renormalization groups*, Phys. Rev. Lett. **69**, 2863 (1992), doi:[10.1103/PhysRevLett.69.2863](https://doi.org/10.1103/PhysRevLett.69.2863).
- [5] I. V. Oseledets, *Tensor-train decomposition*, SIAM Journal on Scientific Computing **33**(5), 2295 (2011), doi:[10.1137/090752286](https://doi.org/10.1137/090752286), <https://doi.org/10.1137/090752286>.
- [6] I. V. Oseledets, *Constructive representation of functions in low-rank tensor formats*, Constructive Approximation **37**(1), 1 (2013), doi:[10.1007/s00365-012-9175-x](https://doi.org/10.1007/s00365-012-9175-x).
- [7] B. N. Khoromskij, *Tensor Numerical Methods in Scientific Computing*, De Gruyter, Berlin, Boston, ISBN 9783110365917, doi:[doi:10.1515/9783110365917](https://doi.org/10.1515/9783110365917) (2018).
- [8] B. N. Khoromskij, *$O(d \log n)$ -quantics approximation of n -d tensors in high-dimensional numerical modeling*, Constructive Approximation **34**(2), 257 (2011), doi:[10.1007/s00365-011-9131-1](https://doi.org/10.1007/s00365-011-9131-1).
- [9] I. V. Oseledets, *Approximation of matrices with logarithmic number of parameters*, Doklady Mathematics **80**(2), 653 (2009), doi:[10.1134/S1064562409050056](https://doi.org/10.1134/S1064562409050056).
- [10] S. Dolgov, B. Khoromskij and D. Savostyanov, *Superfast fourier transform using qtt approximation*, Journal of Fourier Analysis and Applications **18**(5), 915 (2012).
- [11] J. Chen, E. Stoudenmire and S. R. White, *Quantum fourier transform has small entanglement*, PRX Quantum **4**, 040318 (2023), doi:[10.1103/PRXQuantum.4.040318](https://doi.org/10.1103/PRXQuantum.4.040318).
- [12] H. Shinaoka, M. Wallerberger, Y. Murakami, K. Nogaki, R. Sakurai, P. Werner and A. Kauch, *Multiscale space-time ansatz for correlation functions of quantum systems based on quantics tensor trains*, Phys. Rev. X **13**, 021015 (2023), doi:[10.1103/PhysRevX.13.021015](https://doi.org/10.1103/PhysRevX.13.021015).

- [13] Y. Núñez Fernández, M. Jeannin, P. T. Dumitrescu, T. Kloss, J. Kaye, O. Parcollet and X. Waintal, *Learning feynman diagrams with tensor trains*, Phys. Rev. X **12**, 041018 (2022), doi:[10.1103/PhysRevX.12.041018](https://doi.org/10.1103/PhysRevX.12.041018).
- [14] H. Takahashi, R. Sakurai and H. Shinaoka, *Compactness of quantics tensor train representations of local imaginary-time propagators*, SciPost Phys. **18**, 007 (2025), doi:[10.21468/SciPostPhys.18.1.007](https://doi.org/10.21468/SciPostPhys.18.1.007).
- [15] B. N. Khoromskij, *Tensor numerical methods for high-dimensional pdes: Basic theory and initial applications*, arXiv preprint arXiv:1408.4053 (2014).
- [16] J. J. García-Ripoll, *Quantum-inspired algorithms for multivariate analysis: from interpolation to partial differential equations*, Quantum **5**, 431 (2021).
- [17] N. Jolly, Y. N. Fernández and X. Waintal, *Tensorized orbitals for computational chemistry* (2024), [2308.03508](https://arxiv.org/abs/2308.03508).
- [18] R. Dilip, Y.-J. Liu, A. Smith and F. Pollmann, *Data compression for quantum machine learning*, Phys. Rev. Res. **4**, 043007 (2022), doi:[10.1103/PhysRevResearch.4.043007](https://doi.org/10.1103/PhysRevResearch.4.043007).
- [19] M. K. Ritter, Y. Núñez Fernández, M. Wallerberger, J. von Delft, H. Shinaoka and X. Waintal, *Quantics tensor cross interpolation for high-resolution parsimonious representations of multivariate functions*, Phys. Rev. Lett. **132**, 056501 (2024), doi:[10.1103/PhysRevLett.132.056501](https://doi.org/10.1103/PhysRevLett.132.056501).
- [20] P. García-Molina, L. Tagliacozzo and J. J. García-Ripoll, *Global optimization of mps in quantum-inspired numerical analysis*, arXiv preprint arXiv:2303.09430 (2023).
- [21] J.-W. Li and X. Waintal, *Matrix product states and first quantization* (2024), [2404.07105](https://arxiv.org/abs/2404.07105).
- [22] J. Haegeman, J. I. Cirac, T. J. Osborne, I. Pižorn, H. Verschelde and F. Verstraete, *Time-dependent variational principle for quantum lattices*, Phys. Rev. Lett. **107**, 070601 (2011), doi:[10.1103/PhysRevLett.107.070601](https://doi.org/10.1103/PhysRevLett.107.070601).
- [23] J. Haegeman, C. Lubich, I. Oseledets, B. Vandereycken and F. Verstraete, *Unifying time evolution and optimization with matrix product states*, Phys. Rev. B **94**, 165116 (2016), doi:[10.1103/PhysRevB.94.165116](https://doi.org/10.1103/PhysRevB.94.165116).
- [24] J. Rogel-Salazar, *The gross-pitaevskii equation and bose-einstein condensates*, European Journal of Physics **34**(2), 247 (2013).
- [25] A. Einstein, *Quantum theory of the monatomic ideal gas*, Sitzungsberichte der Preussischen Akademie der Wissenschaften, Physikalisch-mathematische Klasse **261**, 44 (1924).
- [26] Y.-j. Lin, I. Teper, C. Chin and V. Vuletic, *Impact of the Casimir-Polder Potential and Johnson Noise on Bose-Einstein Condensate Stability Near Surfaces*, Phys. Rev. Lett. **92**, 050404 (2004), doi:[10.1103/PhysRevLett.92.050404](https://doi.org/10.1103/PhysRevLett.92.050404), [cond-mat/0308457](https://arxiv.org/abs/cond-mat/0308457).
- [27] M. H. Anderson, J. R. Ensher, M. R. Matthews, C. E. Wieman and E. A. Cornell, *Observation of bose-einstein condensation in a dilute atomic vapor*, Science **269**(5221), 198 (1995), doi:[10.1126/science.269.5221.198](https://doi.org/10.1126/science.269.5221.198), <https://www.science.org/doi/pdf/10.1126/science.269.5221.198>.
- [28] F. Dalfovo, S. Giorgini, L. P. Pitaevskii and S. Stringari, *Theory of bose-einstein condensation in trapped gases*, Rev. Mod. Phys. **71**, 463 (1999), doi:[10.1103/RevModPhys.71.463](https://doi.org/10.1103/RevModPhys.71.463).

- [29] J. R. Abo-Shaeer, C. Raman, J. M. Vogels and W. Ketterle, *Observation of vortex lattices in bose-einstein condensates*, *Science* **292**(5516), 476 (2001).
- [30] Z. Hadzibabic, P. Krüger, M. Cheneau, B. Battelier and J. Dalibard, *Berezinskii–Kosterlitz–Thouless crossover in a trapped atomic gas*, *Nature* **441**(7097), 1118 (2006), doi:[10.1038/nature04851](https://doi.org/10.1038/nature04851).
- [31] C. Chin, R. Grimm, P. Julienne and E. Tiesinga, *Feshbach resonances in ultracold gases*, *Rev. Mod. Phys.* **82**, 1225 (2010), doi:[10.1103/RevModPhys.82.1225](https://doi.org/10.1103/RevModPhys.82.1225).
- [32] K. W. Madison, F. Chevy, W. Wohlleben and J. Dalibard, *Vortex formation in a stirred bose-einstein condensate*, *Phys. Rev. Lett.* **84**, 806 (2000), doi:[10.1103/PhysRevLett.84.806](https://doi.org/10.1103/PhysRevLett.84.806).
- [33] F. Gerbier and J. Dalibard, *Gauge fields for ultracold atoms in optical superlattices*, *New J. Phys.* **12**, 033007 (2010), doi:[10.1088/1367-2630/12/3/033007](https://doi.org/10.1088/1367-2630/12/3/033007), [0910.4606](https://arxiv.org/abs/0910.4606).
- [34] S. Donadello, S. Serafini, M. Tylutki, L. P. Pitaevskii, F. Dalfovo, G. Lamporesi and G. Ferrari, *Observation of solitonic vortices in bose-einstein condensates*, *Phys. Rev. Lett.* **113**, 065302 (2014), doi:[10.1103/PhysRevLett.113.065302](https://doi.org/10.1103/PhysRevLett.113.065302).
- [35] M. R. Matthews, B. P. Anderson, P. C. Haljan, D. S. Hall, C. E. Wieman and E. A. Cornell, *Vortices in a bose-einstein condensate*, *Phys. Rev. Lett.* **83**, 2498 (1999), doi:[10.1103/PhysRevLett.83.2498](https://doi.org/10.1103/PhysRevLett.83.2498).
- [36] A. Karailiev, M. Gazo, M. Gałka, C. Eigen, T. Satoor and Z. Hadzibabic, *Observation of an Inverse Turbulent-Wave Cascade in a Driven Quantum Gas*, *Phys. Rev. Lett.* **133**(24), 243402 (2024), doi:[10.1103/PhysRevLett.133.243402](https://doi.org/10.1103/PhysRevLett.133.243402), [2405.01537](https://arxiv.org/abs/2405.01537).
- [37] Y. Geng, S. Mukherjee, S. Banik, M. G. Galan, M. J. Anderson, H. Sosa-Martinez, S. P. Eckel, I. B. Spielman and G. K. Campbell, *Efficient production of sodium Bose-Einstein condensates in a hybrid trap* (2025), [2505.21415](https://arxiv.org/abs/2505.21415).
- [38] C. F. Barenghi, L. Skrbek and K. R. Sreenivasan, *Quantum turbulence*, Cambridge University Press (2023).
- [39] N. P. Proukakis, *A century of bose-einstein condensation*, *Communications Physics* **8**(1), 264 (2025).
- [40] I. M. Georgescu, S. Ashhab and F. Nori, *Quantum simulation*, *Rev. Mod. Phys.* **86**, 153 (2014), doi:[10.1103/RevModPhys.86.153](https://doi.org/10.1103/RevModPhys.86.153).
- [41] L. Amico, M. Boshier, G. Birkl, A. Minguzzi, C. Miniatura, L.-C. Kwek, D. Aghamalyan, V. Ahufinger, D. Anderson, N. Andrei *et al.*, *Roadmap on atomtronics: State of the art and perspective*, *AVS Quantum Science* **3**(3) (2021).
- [42] A. Minguzzi, S. Succi, F. Toschi, M. P. Tosi and P. Vignolo, *Numerical methods for atomic quantum gases with applications to Bose-Einstein condensates and to ultracold fermions*, *Physics reports* **395**(4-5), 223 (2004), doi:[10.1016/j.physrep.2004.02.001](https://doi.org/10.1016/j.physrep.2004.02.001).
- [43] P. Henning and E. Jarlebring, *The gross–pitaevskii equation and eigenvector nonlinearities: numerical methods and algorithms*, *SIAM Review* **67**(2), 256 (2025).
- [44] W. Bao, D. Jaksch and P. A. Markowich, *Numerical solution of the gross–pitaevskii equation for bose–einstein condensation*, *Journal of Computational Physics* **187**(1), 318 (2003).

- [45] M. Modugno, L. Pricoupenko and Y. Castin, *Bose-Einstein condensates with a bent vortex in rotating traps*, European Physical Journal D **22**(2), 235 (2003), doi:[10.1140/epjd/e2003-00015-y](https://doi.org/10.1140/epjd/e2003-00015-y), [cond-mat/0203597](https://arxiv.org/abs/cond-mat/0203597).
- [46] T. Winiecki, *Numerical studies of superfluids and superconductors*, Ph.D Thesis (2001).
- [47] T. Bland, M. J. Edmonds, N. P. Proukakis, A. M. Martin, D. H. J. O'Dell and N. G. Parker, *Controllable nonlocal interactions between dark solitons in dipolar condensates*, Phys. Rev. A **92**, 063601 (2015), doi:[10.1103/PhysRevA.92.063601](https://doi.org/10.1103/PhysRevA.92.063601).
- [48] I. Danaila and B. Protas, *Computation of ground states of the gross-pitaevskii functional via riemannian optimization*, SIAM Journal on Scientific Computing **39**(6), B1102 (2017).
- [49] H. Chen, G. Dong, W. Liu and Z. Xie, *Second-order flows for computing the ground states of rotating bose-einstein condensates*, Journal of Computational Physics **475**, 111872 (2023).
- [50] J. Gaidamour, Q. Tang and X. Antoine, *Bec2hpc: A hpc spectral solver for nonlinear schrödinger and rotating gross-pitaevskii equations. stationary states computation*, Computer Physics Communications **265**, 108007 (2021), doi:<https://doi.org/10.1016/j.cpc.2021.108007>.
- [51] Y. Xu, Z. Chen, H. Xiong, W. V. Liu and B. Wu, *Stability of p-orbital bose-einstein condensates in optical checkerboard and square lattices*, Phys. Rev. A **87**, 013635 (2013), doi:[10.1103/PhysRevA.87.013635](https://doi.org/10.1103/PhysRevA.87.013635).
- [52] X. Wu, Z. Wen and W. Bao, *A regularized newton method for computing ground states of bose-einstein condensates*, Journal of Scientific Computing **73**, 303 (2017).
- [53] J.-S. You, I.-K. Liu, D.-W. Wang, S.-C. Gou and C. Wu, *Unconventional bose-einstein condensation in a system with two species of bosons in the p-orbital bands in an optical lattice*, Phys. Rev. A **93**, 053623 (2016), doi:[10.1103/PhysRevA.93.053623](https://doi.org/10.1103/PhysRevA.93.053623).
- [54] X. Antoine and R. Duboscq, *Gpelab, a matlab toolbox to solve gross-pitaevskii equations i: Computation of stationary solutions*, Computer Physics Communications **185**(11), 2969 (2014).
- [55] P. B. Blakie, *Numerical method for evolving the projected gross-pitaevskii equation*, Phys. Rev. E **78**, 026704 (2008), doi:[10.1103/PhysRevE.78.026704](https://doi.org/10.1103/PhysRevE.78.026704).
- [56] S. J. Rooney, P. B. Blakie and A. S. Bradley, *Numerical method for the stochastic projected gross-pitaevskii equation*, Phys. Rev. E **89**, 013302 (2014), doi:[10.1103/PhysRevE.89.013302](https://doi.org/10.1103/PhysRevE.89.013302).
- [57] N. A. Keeper, I.-K. Liu, F. Dalfovo and N. P. Proukakis, *Phase transition dimensionality crossover from two to three dimensions in a trapped ultracold atomic bose gas*, Phys. Rev. Res. **4**, 033130 (2022), doi:[10.1103/PhysRevResearch.4.033130](https://doi.org/10.1103/PhysRevResearch.4.033130).
- [58] H.-Y. Schive, T. Chiueh and T. Broadhurst, *Cosmic Structure as the Quantum Interference of a Coherent Dark Wave*, Nature Phys. **10**, 496 (2014), doi:[10.1038/nphys2996](https://doi.org/10.1038/nphys2996), [1406.6586](https://doi.org/10.1038/1406.6586).
- [59] S. A. Morgan, S. Choi, K. Burnett and M. Edwards, *Nonlinear mixing of quasi-particles in an inhomogeneous bose condensate*, Phys. Rev. A **57**, 3818 (1998), doi:[10.1103/PhysRevA.57.3818](https://doi.org/10.1103/PhysRevA.57.3818).

- [60] C.-M. Schmied, A. N. Mikheev and T. Gasenzer, *Non-thermal fixed points: Universal dynamics far from equilibrium*, International Journal of Modern Physics A **34**(29), 1941006 (2019).
- [61] G. W. Stagg, N. G. Parker and C. F. Barenghi, *Superfluid boundary layer*, Phys. Rev. Lett. **118**, 135301 (2017), doi:[10.1103/PhysRevLett.118.135301](https://doi.org/10.1103/PhysRevLett.118.135301).
- [62] S. May and V. Springel, *Structure formation in large-volume cosmological simulations of fuzzy dark matter: impact of the non-linear dynamics*, Monthly Notices of the Royal Astronomical Society **506**(2), 2603 (2021).
- [63] I.-K. Liu, A. W. Baggaley, C. F. Barenghi and T. S. Wood, *Vortex Avalanches and Collective Motion in Neutron Stars*, Astrophys. J. **984**(1), 83 (2025), doi:[10.3847/1538-4357/adc383](https://doi.org/10.3847/1538-4357/adc383), [2410.16878](https://arxiv.org/abs/2410.16878).
- [64] W. Bao and Q. Du, *Computing the ground state solution of bose–einstein condensates by a normalized gradient flow*, SIAM Journal on Scientific Computing **25**(5), 1674 (2004), doi:[10.1137/S1064827503422956](https://doi.org/10.1137/S1064827503422956).
- [65] L. M. Symes, R. I. McLachlan and P. B. Blakie, *Efficient and accurate methods for solving the time-dependent spin-1 gross-pitaevskii equation*, Phys. Rev. E **93**, 053309 (2016), doi:[10.1103/PhysRevE.93.053309](https://doi.org/10.1103/PhysRevE.93.053309).
- [66] P. A. Ruprecht, M. J. Holland, K. Burnett and M. Edwards, *Time-dependent solution of the nonlinear schrödinger equation for bose-condensed trapped neutral atoms*, Phys. Rev. A **51**, 4704 (1995), doi:[10.1103/PhysRevA.51.4704](https://doi.org/10.1103/PhysRevA.51.4704).
- [67] R. Kishor Kumar, V. Lončar, P. Muruganandam, S. K. Adhikari and A. Balaž, *C and fortran openmp programs for rotating bose–einstein condensates*, Computer Physics Communications **240**, 74 (2019), doi:<https://doi.org/10.1016/j.cpc.2019.03.004>.
- [68] P. Muruganandam and S. K. Adhikari, *Fortran programs for the time-dependent gross-pitaevskii equation in a fully anisotropic trap*, Computer Physics Communications **180**(10), 1888 (2009).
- [69] X. Antoine and R. Duboscq, *Gpelab, a matlab toolbox to solve gross-pitaevskii equations ii: Dynamics and stochastic simulations*, Computer Physics Communications **193**, 95 (2015).
- [70] L. J. O’Riordan and T. Busch, *Topological defect dynamics of vortex lattices in bose-einstein condensates*, Phys. Rev. A **94**, 053603 (2016), doi:[10.1103/PhysRevA.94.053603](https://doi.org/10.1103/PhysRevA.94.053603).
- [71] P.-H. Chavanis, *Mass-radius relation of newtonian self-gravitating bose-einstein condensates with short-range interactions. i. analytical results*, Phys. Rev. D **84**, 043531 (2011), doi:[10.1103/PhysRevD.84.043531](https://doi.org/10.1103/PhysRevD.84.043531).
- [72] H. Huang, H.-Y. Schive and T. Chiueh, *Cosmological simulations of two-component wave dark matter*, Mon. Not. Roy. Astron. Soc. **522**(1), 515 (2023), doi:[10.1093/mnras/stad998](https://doi.org/10.1093/mnras/stad998), [2212.14288](https://arxiv.org/abs/2212.14288).
- [73] H. Y. J. Chan, H.-Y. Schive, V. H. Robles, A. Kunkel, G.-M. Su and P.-Y. Liao, *Cosmological zoom-in simulation of fuzzy dark matter down to $z = 0$: tidal evolution of subhaloes in a Milky Way-sized halo* (2025), [2504.10387](https://arxiv.org/abs/2504.10387).
- [74] V. Graber, N. Andersson and M. Hogg, *Neutron Stars in the Laboratory*, Int. J. Mod. Phys. D **26**(08), 1730015 (2017), doi:[10.1142/S0218271817300154](https://doi.org/10.1142/S0218271817300154), [1610.06882](https://arxiv.org/abs/1610.06882).

- [75] T. S. Wood and V. Graber, *Superconducting Phases in Neutron Star Cores*, *Universe* **8**(4), 228 (2022), doi:[10.3390/universe8040228](https://doi.org/10.3390/universe8040228).
- [76] A. A. Abrikosov, *On the Magnetic properties of superconductors of the second group*, *Sov. Phys. JETP* **5**, 1174 (1957).
- [77] L. Pitaevskii and S. Stringari, *Bose-Einstein condensation and superfluidity*, vol. 164, Oxford University Press (2016).
- [78] T. Kimura, *Breathing mode collective excitation of a bose-einstein condensate in a low-dimensional trap*, *Physica B: Condensed Matter* **329**, 44 (2003).
- [79] M. Niedermeier, A. Moulinas, T. Louvet, J. L. Lado and X. Waintal, *Solving the gross-pitaevskii equation on multiple different scales using the quantics tensor train representation*, Concurrent independent work, to appear on arXiv (2025).
- [80] A. Bou-Comas, M. Płodzień, L. Tagliacozzo and J. J. García-Ripoll, *Quantics tensor train for solving gross-pitaevskii equation* (2025), [2507.03134](https://arxiv.org/abs/2507.03134).
- [81] R. J. J. Co, C. W. Duncan and A. J. Daley, *Tensor network methods for the gross-pitaevskii equation on fine grids* (2025), [2507.01149](https://arxiv.org/abs/2507.01149).
- [82] N. Cooper, *Rapidly rotating atomic gases*, *Advances in Physics* **57**(6), 539 (2008), doi:[10.1080/00018730802564122](https://doi.org/10.1080/00018730802564122), <https://doi.org/10.1080/00018730802564122>.
- [83] L. Vanderstraeten, J. Haegeman and F. Verstraete, *Tangent-space methods for uniform matrix product states*, *SciPost Phys. Lect. Notes* p. 7 (2019), doi:[10.21468/SciPostPhysLectNotes.7](https://doi.org/10.21468/SciPostPhysLectNotes.7).
- [84] M. Hauru, M. V. Damme and J. Haegeman, *Riemannian optimization of isometric tensor networks*, *SciPost Phys.* **10**, 040 (2021), doi:[10.21468/SciPostPhys.10.2.040](https://doi.org/10.21468/SciPostPhys.10.2.040).
- [85] X. Zhu, *A riemannian conjugate gradient method for optimization on the stiefel manifold*, *Computational Optimization and Applications* **67**(1), 73 (2017), doi:[10.1007/s10589-016-9883-4](https://doi.org/10.1007/s10589-016-9883-4).
- [86] T. Abrudan, J. Eriksson and V. Koivunen, *Conjugate gradient algorithm for optimization under unitary matrix constraint*, *Signal Processing* **89**(9), 1704 (2009), doi:<https://doi.org/10.1016/j.sigpro.2009.03.015>.
- [87] J.-W. Li, J. von Delft and H.-H. Tu, *$U(1)$ -symmetric gaussian fermionic projected entangled paired states and their gutzwiller projection*, *Phys. Rev. B* **107**, 085148 (2023), doi:[10.1103/PhysRevB.107.085148](https://doi.org/10.1103/PhysRevB.107.085148).
- [88] C. Trallero-Giner, M. V. Durnev, Y. N. n. Fernández, M. I. Vasilevskiy, V. López-Richard and A. Kavokin, *Excited states of exciton-polariton condensates in 2d and 1d harmonic traps*, *Phys. Rev. B* **89**, 205317 (2014), doi:[10.1103/PhysRevB.89.205317](https://doi.org/10.1103/PhysRevB.89.205317).
- [89] H. Zhai, *Ultracold atomic physics*, Cambridge University Press (2021).
- [90] I. Oseledets and E. Tyrtshnikov, *Tt-cross approximation for multidimensional arrays*, *Linear Algebra and its Applications* **432**(1), 70 (2010), doi:<https://doi.org/10.1016/j.laa.2009.07.024>.
- [91] D. Savostyanov and I. Oseledets, *Fast adaptive interpolation of multi-dimensional arrays in tensor train format*, In *The 2011 International Workshop on Multidimensional (nD) Systems*, pp. 1–8, doi:[10.1109/nDS.2011.6076873](https://doi.org/10.1109/nDS.2011.6076873) (2011).

- [92] D. V. Savostyanov, *Quasioptimality of maximum-volume cross interpolation of tensors*, *Linear Algebra and its Applications* **458**, 217 (2014), doi:<https://doi.org/10.1016/j.laa.2014.06.006>.
- [93] S. Dolgov and D. Savostyanov, *Parallel cross interpolation for high-precision calculation of high-dimensional integrals*, *Computer Physics Communications* **246**, 106869 (2020), doi:<https://doi.org/10.1016/j.cpc.2019.106869>.
- [94] Y. N. Fernández, M. K. Ritter, M. Jeannin, J.-W. Li, T. Kloss, T. Louvet, S. Terasaki, O. Parcollet, J. von Delft, H. Shinaoka *et al.*, *Learning tensor networks with tensor cross interpolation: new algorithms and libraries*, arXiv preprint arXiv:2407.02454 (2024).